



Fiberized Diamond-Based Vector Magnetometers

Georgios Chatzidrosos^{1,2*}, Joseph Shaji Rebeirro^{1,2}, Huijie Zheng^{1,2*}, Muhib Omar^{1,2}, Andreas Brenneis³, Felix M. Stürner³, Tino Fuchs³, Thomas Buck³, Robert Röfver³, Tim Schneemann^{1,2}, Peter Blümler², Dmitry Budker^{1,2,4} and Arne Wickenbrock^{1,2}

¹Helmholtz-Institut, GSI Helmholtzzentrum für Schwerionenforschung, Mainz, Germany, ²Department of Physics, Johannes Gutenberg-Universität Mainz, Mainz, Germany, ³Corporate Sector Research and Advance Engineering, Robert Bosch GmbH, Renningen, Germany, ⁴Department of Physics, University of California, Berkeley, Berkeley, CA, United States

OPEN ACCESS

Edited by:

Eilon Poem,
Weizmann Institute of Science, Israel

Reviewed by:

Jonas Nils Becker,
Imperial College London,
United Kingdom
Anton Vershovskii,
Ioffe Institute (RAS), Russia
Xing Rong,
University of Science and Technology
of China, China

*Correspondence:

Georgios Chatzidrosos
gechatzi@uni-mainz.de
Huijie Zheng
zheng@uni-mainz.de

Specialty section:

This article was submitted to
Quantum Optics,
a section of the journal
Frontiers in Photonics

Received: 29 June 2021

Accepted: 10 August 2021

Published: 20 August 2021

Citation:

Chatzidrosos G, Rebeirro JS, Zheng H,
Omar M, Brenneis A, Stürner FM,
Fuchs T, Buck T, Röfver R,
Schneemann T, Blümler P, Budker D
and Wickenbrock A (2021) Fiberized
Diamond-Based
Vector Magnetometers.
Front. Photonics 2:732748.
doi: 10.3389/fphot.2021.732748

We present two fiberized vector magnetic-field sensors, based on nitrogen-vacancy (NV) centers in diamond. The sensors feature sub-nT/ $\sqrt{\text{Hz}}$ magnetic sensitivity. We use commercially available components to construct sensors with a small sensor size, high photon collection, and minimal sensor-sample distance. Both sensors are located at the end of optical fibres with the sensor-head freely accessible and robust under movement. These features make them ideal for mapping magnetic fields with high sensitivity and spatial resolution (\leq mm). As a demonstration we use one of the sensors to map the vector magnetic field inside the bore of a ≥ 100 mT Halbach array. The vector field sensing protocol translates microwave spectroscopy data addressing all diamonds axes and including double quantum transitions to a 3D magnetic field vector.

Keywords: NV, nitrogen-vacancy, magnetometers, vector magnetometry, quantum sensing, fiberized system, nitrogen-vacancy (NV) center

1 INTRODUCTION

Nitrogen-vacancy (NV) centers in diamond have attracted attention as magnetic field sensors with high spatial resolution (Balasubramanian et al., 2008; Maze et al., 2008; Rittweger et al., 2009) and sensitivity (Barry et al., 2016; Chatzidrosos et al., 2017; Zhang et al., 2021). Their sensitivity has been demonstrated to be as low as sub-pT level, for AC fields (Wolf et al., 2015) and with hybrid magnetometers at the low-frequency regime (Xie et al., 2021) The range of their application includes, but is not limited to, single neuron-action potential detection (Barry et al., 2016), single protein spectroscopy (Lovchinsky et al., 2016), as well as *in vivo* thermometry (Kucsko et al., 2013). Advantages of NV-based magnetometers, compared to other magnetic field sensors, include their ability to operate in wide temperature and magnetic field ranges (Zheng et al., 2017). The ability to operate them also without the use of microwaves (Wickenbrock et al., 2016; Zheng et al., 2017; Zheng et al., 2020), has recently enabled a variety of new applications in environments where microwaves (MW) would be detrimental (Chatzidrosos et al., 2019).

The NV consists of a substitutional nitrogen and an adjacent vacant carbon site. It can appear in different orientations along the crystallographic axes of the diamond lattice. This enables vector measurements of magnetic fields (Clevenson et al., 2018). Vector magnetometry itself can be useful in magnetic navigation applications (Cochrane et al., 2016), magnetic anomaly detection, current and position sensing, and the measurement of biological magnetic fields (Barry et al., 2016). Vector measurements near a background field of ~ 100 mT, where the NV's ground state level anti-crossing (GSLAC) occurs, are of particular interest (Zheng et al., 2020). Some of the challenges of vector measurements near the GSLAC field include the necessity to precisely align the NV and the bias

magnetic field axes for optimum sensitivity of the microwave-free method (Zheng et al., 2017) or the need to account for transversal field related nonlinearities of the NV gyromagnetic ratio when performing microwave spectroscopy.

One of the challenges NV magnetometers face is their low photon-collection efficiency. Approaches to increase the efficiency include, use of solid immersion lenses (Hadden et al., 2010; Siyushev et al., 2010; Sage et al., 2012), or employment of infrared absorption (Acosta et al., 2010; Dumeige et al., 2013; Jensen et al., 2014; Chatzidrosos et al., 2017; Dumeige et al., 2019). Photoluminescence (PL) for fiberized sensors is preferentially collected with the same fiber delivering the pump light but detected on the input side of the fiber (Patel et al., 2020). Despite considerable effort, even modern sensors typically just feature a PL-to-pump-light ratio of about 0.1% (Barry et al., 2016; Patel et al., 2020).

In this paper, we discuss the construction of a fiberized NV-based vector magnetic field sensors and compare it with another sensor of the same kind. One sensor is constructed in Helmholtz Institute Mainz, referred to as Mainz sensor in the following and the other one is constructed by Robert Bosch GmbH, referred to as Bosch sensor in the following. They both achieve sub $\text{nT}/\sqrt{\text{Hz}}$ magnetic sensitivity. The sensor constructed in Mainz achieved a sensitivity of $0.45 \text{ nT}/\sqrt{\text{Hz}}$, limited by intensity noise of the pump laser, with $11 \text{ pT}/\sqrt{\text{Hz}}$ photon-shot noise sensitivity and 0.5% PL-to-pump power ratio taking the fiber coupling efficiency into account. The sensor constructed by Bosch achieved a sensitivity of $0.34 \text{ nT}/\sqrt{\text{Hz}}$, which was approximately one order of magnitude larger than the expected photon-shot noise limited sensitivity (Stürner et al., 2021). The PL-to-pump power ratio was 0.3% taking the fiber-coupling efficiency into account. The components used for the construction of both sensors are commercially available. They allow for a small sensor size ($11 \times 40 \text{ mm}^2$ for Mainz and $15 \times 25 \text{ mm}^2$ for Bosch) with maximized PL-to-pump-light ratio, as well as robustness to movement, which also makes the sensors portable. All of this makes the sensors ideal for mapping magnetic fields and measuring in regions that are not easily accessible. The magnetometers are constructed in such a way that they allow close proximity of the sensors to magnetic field sources, thus allowing for high spatial resolution when mapping magnetic fields. After demonstrating the sensitivity of the sensors and explaining the principles of vector magnetometry with NV centers, we used the Mainz sensor to perform spatially resolved optically detected magnetic resonance (ODMR) measurements covering an area of $\times 20 \text{ 30 mm}^2$ inside a Halbach-magnet array. The Halbach array itself provides a highly homogeneous magnetic field around 100 mT which makes it ideal for near-GSLAC magnetic field measurements and studies with NV centers. We present the analysis for the translation of the extracted frequency measurements into magnetic field. Details about the construction of the highly homogeneous Halbach array is subject of another publication (Wickenbrock et al., 2020).

2 EXPERIMENTAL SETUP

The diamond sample used for the Mainz sensor is a $2.0 \times 2.0 \times 0.5 \text{ mm}^3$ type Ib (100)-cut, high-pressure high-temperature

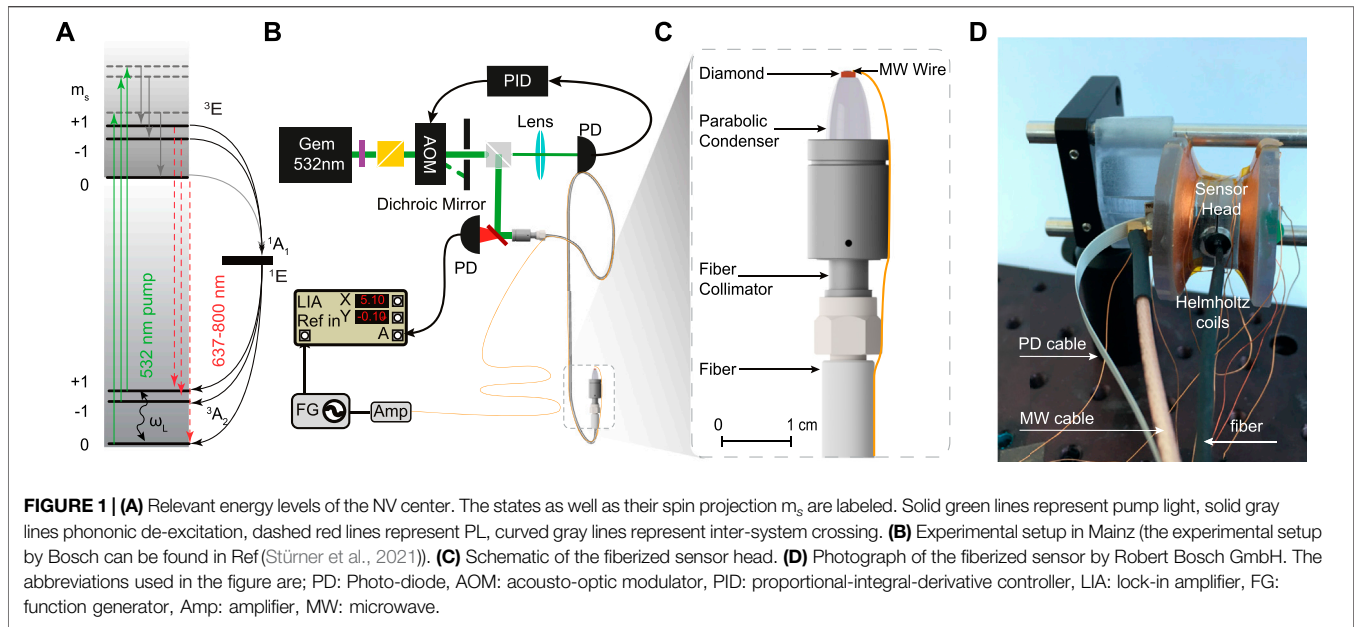
(HPHT) grown sample, purchased from Element Six. The initial [N] concentration of the sample was specified as $< 10 \text{ ppm}$. The sample was irradiated with 5 MeV electrons at a dose of $2 \times 10^{19} \text{ cm}^{-2}$ and then annealed at 700°C for 8 h. The diamond sample used for the Bosch sensor is a $0.8 \times 0.8 \times 0.5 \text{ mm}^3$ (111)-cut, 99.97% ^{12}C enriched, HPHT grown diamond. The sample was irradiated with 2 MeV electrons at a dose of $2 \times 10^{18} \text{ cm}^{-2}$ at room temperature and then annealed at $1,000^\circ\text{C}$ for 2 h in vacuum. The $[\text{NV}^-]$ concentration was determined by electron spin resonance to be 0.4 ppm (Stürner et al., 2021).

Figure 1A shows the relevant energy levels of the negatively charged NV center, which we use for magnetometry. The ground and excited spin-triplet states of the NV are labeled $^3\text{A}_2$ and ^3E , respectively [**Figure 1A**], the transition between them has a zero-phonon line at 637 nm, but can be excited by more energetic photons (of shorter wavelengths) due to phonon excitation in the diamond lattice. The lower and upper electronic singlet states are ^1E and $^1\text{A}_1$, respectively. While optical transition rates are spin-independent, the probability of nonradiative intersystem crossing from ^3E to the singlets is several times higher (Dumeige et al., 2013) for $m_s = \pm 1$ than that for $m_s = 0$. As a consequence, under continuous illumination with green pump light (532 nm), NV centers accumulate mostly in the $^3\text{A}_2, m_s = 0$ ground state sublevel and in the metastable ^1E singlet state. For metrology applications, the spins in the $^3\text{A}_2$ ground state can be coherently manipulated with microwave fields.

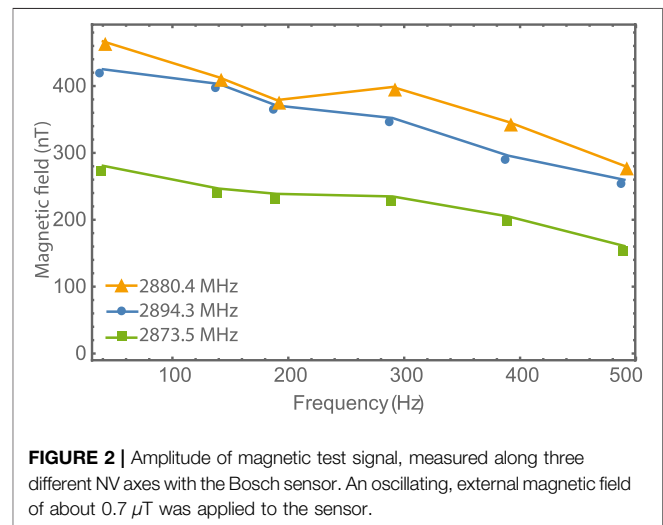
Figure 1B shows the experimental setup used for the measurements conducted in Mainz. To initialize the NV centers to the ground-triplet state, we use a 532 nm (green) laser (Laser Quantum, gem532). To reduce intensity noise from the laser source, the light intensity is stabilized using an acousto-optic modulator (AOM, ISOMET-1260C with an ISOMET 630C-350 driver) controlled through a proportional-integral-derivative controller (PID, SIM960), in a feedback loop. The green laser is normally stabilized to a laser power of 200 mW. The green laser is then coupled into a 2 m long, high-power multi-mode fiber cable (Thorlabs, MHP365L02).

The MW to manipulate the NV spins are generated with a MW function generator (FG; SRS, SG394). They are amplified with a 16 W amplifier (Amp; Mini-Circuits, ZHL-16W-43+) and passed through a circulator (Mini-Circuits, CS-3.000) before they are applied to the NV centers using a mm-sized wire loop. The other side of the wire is directly connected to ground. The radius of the wire used for the wire loop is $50 \mu\text{m}$. The wire is then attached to the optical fiber allowing the two parts to move together. For the magnetic resonance measurements presented in this paper, the MW frequency was scanned between 3,800 MHz and 5,000 MHz. Information on the experimental setup used to conduct the measurements with the Bosch sensor can be found in Ref (Stürner et al., 2021). The data presented for the Bosch sensor are acquired at 20 mW of pump-light power and 0.06 mW of MW power.

A schematic of the Mainz fiberized magnetic field sensor head is shown in **Figure 1C**. The diamond is glued to a parabolic condenser lens, which itself is glued onto a 11 mm focal length lens and attached to a fiber collimator (Thorlabs, F220SMA-532) to which the high-power multi-mode fiber (Thorlabs,



MHP365L02) is connected. The MW wire loop is attached to the other side of the diamond to provide the rapidly oscillating magnetic fields required for this magnetic field detection scheme. The light is delivered to the diamond via the parabolic condenser, lens, collimator and the high-power fiber. The same components collect the spin-state-dependent red PL of the NV ensemble. On the other side of the fibre the PL is filtered using a longpass dichroic filter (Thorlabs, DMLP605) which is also used to couple the incoming green light into the fiber. After the dichroic filter residual reflected green light is removed by a notch filter (Thorlabs, NF533-17) and the PL is focused onto a photodiode (PD; Thorlabs, PDA36a2). The detected signal with the PD is connected to a lock-in amplifier (LIA; SRS, SR830). With this setup we were able to achieve 0.5% PL-to-pump-light ratio, which is an order-of-magnitude improvement compared to other fiberized sensors (Patel et al., 2020). A photograph of the Bosch sensor can be seen in **Figure 1D**. The sensor head, containing a microwave resonator, a custom designed balanced photodetector, and the diamond, which was glued to the collimated output of a single-mode fiber, is located inside a custom designed Helmholtz coil. The Helmholtz coil was used to generate a magnetic bias field of 1.07 mT and the collimation of the laser beam was achieved with a gradient-index lens (GRIN). Further details on the setup used for the Bosch sensor can be found in Ref. (Stürner et al., 2021). The final sensor head, of the Mainz sensor, has a diameter of ≤ 11 mm and a height of 40 mm, in a configuration that allows for $\leq 300 \mu\text{m}$ average distance between sample and sensor, these dimensions refer to not just the NV-containing diamond but to the overall sensor-head footprint, including parabolic lens and fiber collimator. The 2 m long fiber with the attached MW wire and the fiberized sensor head for the Mainz sensor (shown in **Figure 1C**) can be moved independently of the other components. The footprint of the sensor head of the Bosch sensor was $15 \times 25 \text{ mm}^2$, with these dimensions referring to the sensor-head as well. The smallest



distance between the center of the diamond and the outer surface is roughly 2.4 mm, the sensor can move independently as well. To filter low-frequency systematic noise components, e.g. laser-power fluctuations, the MW-frequency ω_L is modulated and the detected PL is demodulated with the LIA. To produce the magnetic field maps presented here, the Mainz sensor assembly was mounted on a computer-controlled motorized 3D translation stage (Thorlabs, MTS25/M-Z8) in the center of the Halbach array (not shown in **Figure 1**).

3 MAGNETIC FIELD SENSITIVITY

Figure 2 depicts the response of the Bosch sensor for three different NV axes upon application of an AC magnetic field with varying frequencies and a constant amplitude of $0.7 \mu\text{T}$. The three

TABLE 1 | Settings and detection limit for the three different NV axis used in the Bosch sensor.

f_{res}	f_{mod}	f_{depth}	Detection limit
2,880.4 MHz	3 kHz	100 kHz	$3.7 \pm 0.6 \text{ nT}/\sqrt{\text{Hz}}$
2,894.3 MHz	2 kHz	100 kHz	$3.1 \pm 0.3 \text{ nT}/\sqrt{\text{Hz}}$
2,873.5 MHz	5 kHz	100 kHz	$2.7 \pm 1.6 \text{ nT}/\sqrt{\text{Hz}}$

axes see different effective amplitudes due to the different angles of the NV axes with respect to the magnetic field vector as expected. The sensor response slightly decreases with increasing frequency of the test field independent of the axis. This decrease might stem from the fact, that with increasing frequency, the excitation field becomes under-sampled meaning that the full reconstruction of the sinusoidal excitation field is not possible anymore leading to a decrease in measured amplitude. This decrease is not observable for the Mainz sensor, whose bandwidth is currently limited by the integration constant of the lock-in amplifier used during data acquisition.

To estimate the magnetic sensitivity of the two sensors we follow another method. When the MW field is resonant with the ground-state $m_s = 0 \rightarrow m_s = \pm 1$ transitions, population is transferred through the excited triplet state to the metastable singlet state, resulting in PL reduction. PL as a function of MW frequency is the ODMR signal. By focusing around a single of feature in this ODMR signal the sensitivity can be extracted. The magnetic resonance for the Mainz sensor features a 350 kHz linewidth and 1.6% contrast. The best sensitivity of the Bosch sensor was achieved with a linewidth of ≈ 92 kHz and a contrast of 0.6%. We modulate the MW frequency around a central frequency f_c , and record the first harmonic of the transmission signal with a LIA. This generates a demodulated signal, which together with the NV gyromagnetic ratio of $|^{\gamma}/2\pi| \sim 28.024 \text{ GHz T}^{-1}$ can be used to translate PL fluctuations to effective magnetic field noise. The optimized parameters resulting in the best magnetic field sensitivity for the Mainz sensor were: a modulation frequency of $f_{mod} = 13.6$ kHz and modulation amplitude of $f_{amp} = 260$ kHz. The sensitivity of the Bosch sensor was optimized for three different NV axes as summarized in **Table 1**.

Figure 3 shows the magnetic-field-noise spectrum of the sensors. The blue trace of **Figure 3** corresponds to magnetically sensitive data of the Mainz sensor, the orange to magnetically insensitive. The magnetically sensitive data are taken at a MW frequency resonant with the NV electronic sublevels, while magnetically insensitive data are taken off resonance. The purple and green trace correspond to magnetically sensitive spectrum of the Bosch sensor outside and inside a magnetic shield, respectively, finally the red trace corresponds to the insensitive plot. The magnetically insensitive spectrum can be obtained if f_c is selected to be far from the ODMR features. The peak at 50 Hz is attributed to magnetic field from the power line in the lab. The average sensitivity in the 60–90 Hz area is $0.45 \text{ nT}/\sqrt{\text{Hz}}$ and $0.34 \text{ nT}/\sqrt{\text{Hz}}$, it is achieved for pump light power of 100 and 20 mW, for the Mainz and Bosch sensors respectively.

The noise traces for the Bosch sensor are based on continuous data series, that are recorded with a sampling rate of 1 kHz for 100 s. To calculate the amplitude spectral density (ASD), the data series was split in 100 consecutive intervals, each with a duration of 1 s. For each interval the ASD was calculated. The depicted is the average of the 100 ASDs.

4 VECTOR MAGNETIC FIELD SENSING

4.1 Data Acquisition

As a demonstration of the robustness and portability of our sensors as well as the ability to produce highly resolved magnetic field maps, we select the Mainz sensor to characterize the homogeneity of a custom-made Halbach-array magnet constructed in the Mainz laboratory. The schematic of the magnet is shown in **Figure 4A** with more details found in Ref. (Wickenbrock et al., 2020). It is a double ring of permanent magnets arranged to generate a homogeneous magnetic field in its inner bore along the radius of the rings. The field outside the construction decays rapidly with distance. We performed ODMR measurements in a $30 \times 20 \text{ mm}^2$ plane nearly perpendicular to the main magnetic field direction in the center of the Halbach array in steps of 1 and 1.5 mm in z and y -direction, respectively. The experimental procedure to characterize this magnet involves reconstruction of the 3D magnetic field from these ODMR measurements, which we describe in the next part of this paper. The measurements confirmed the homogeneity of the magnetic field of the magnet to be consistent with Hall-probe and NMR measurements, but with a threefold improved field strength resolution, vector information of the magnetic field and sub-mm spatial information of these quantities. The orientation of the fiberized sensor in the Halbach magnet can be seen in **Figure 4a**.

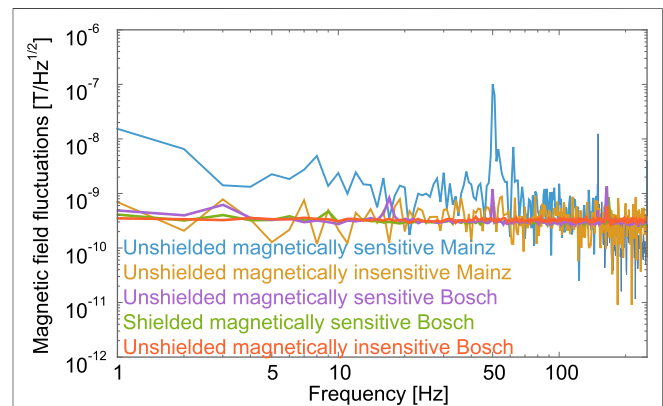
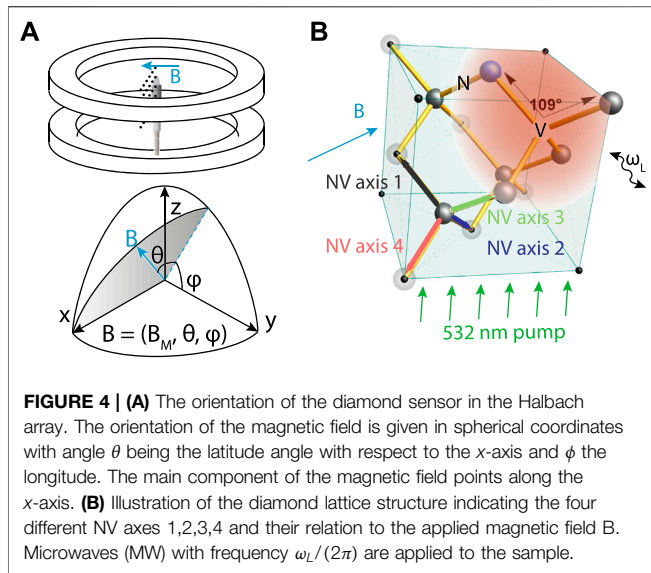


FIGURE 3 | Magnetic field fluctuations measured with the fiberized NV magnetometers. The blue and orange traces depict magnetically sensitive and insensitive data of the Mainz sensor. The purple and green traces correspond to magnetically sensitive spectra of the Bosch sensor outside and inside a magnetic shield, finally, the red trace corresponds to unshielded magnetically insensitive data. The average sensitivity in the 60–90 Hz band is $\text{sub-nT}/\sqrt{\text{Hz}}$. The Bosch data are the result of 100 averages, while the Mainz data is from a single acquisition.



The magnetic field is given in spherical coordinates with respect to the (100) axis of the diamond $B = (B_M, \theta, \phi)$. The angle between the magnetic field vector and the yz -plane is θ , and ϕ is the angle between the projection of B in the yz -plane and the y -axis. The diamond sensor was oriented in the magnetic field such that different resonances were visible.

For each position in the $30 \times 20 \text{ mm}^2$ plane a scan of the applied MW frequency between 3,800 MHz and 5,000 MHz was performed in steps of 1 MHz. This range was limited by the bandwidth of the MW components. At each frequency we recorded the demodulated PL from the LIA x-output with a data acquisition system and stored each data set with its respective position. To speed up the acquisition and after determining that no features were left out, we just acquired in

total 164 frequency values around the expected position of the resonances. In total a frequency scan to determine the four center frequencies lasted 46 s. This can be dramatically improved by for example applying a frequency lock on the four transitions, respectively.

Figure 5 shows an example of collected data in four different points of the scan. The points are noted in Figure 8B with different colors. The four different frequency regions correspond to different kind of transitions as noted above the figures. The FWHM linewidth of the observed features is (11.48 ± 0.14) MHz and therefore much larger than the one given above (0.35 ± 0.02) MHz for a small background field along one of the NV axis. This is due to the strong transverse field component but also caused intentional via MW power broadening. This simplified the lineshape by suppressing the hyperfine features in the spectrum and therefore the analysis routine. We additionally like to note, that the two first of the features are double quantum transitions (DQ), i.e. magnetic transitions from the $m_s = -1$ to the $m_s = +1$ state, normally forbidden, but allowed when transverse magnetic field components are present.

Overall the sensor was moved in steps of 1 and 1.5 mm in z and y -direction, respectively, such that the whole area was covered. The resulting frequency maps of the chosen four resonances can be seen in Figure 8A; they show structures corresponding to the strength of the longitudinal (along the NV axis) and transverse (perpendicular to the NV axis) component of the magnetic field for a given diamond lattice axis. The information contained in these plots is more than sufficient to reconstruct all three vector components of the magnetic field at the position of the sensor.

4.2 Frequency to Vector Field Conversion

After acquiring MW frequency scans for different positions, the data were fitted with the sum of four derivatives of Lorentzians. The four center frequencies, four amplitudes and a combined

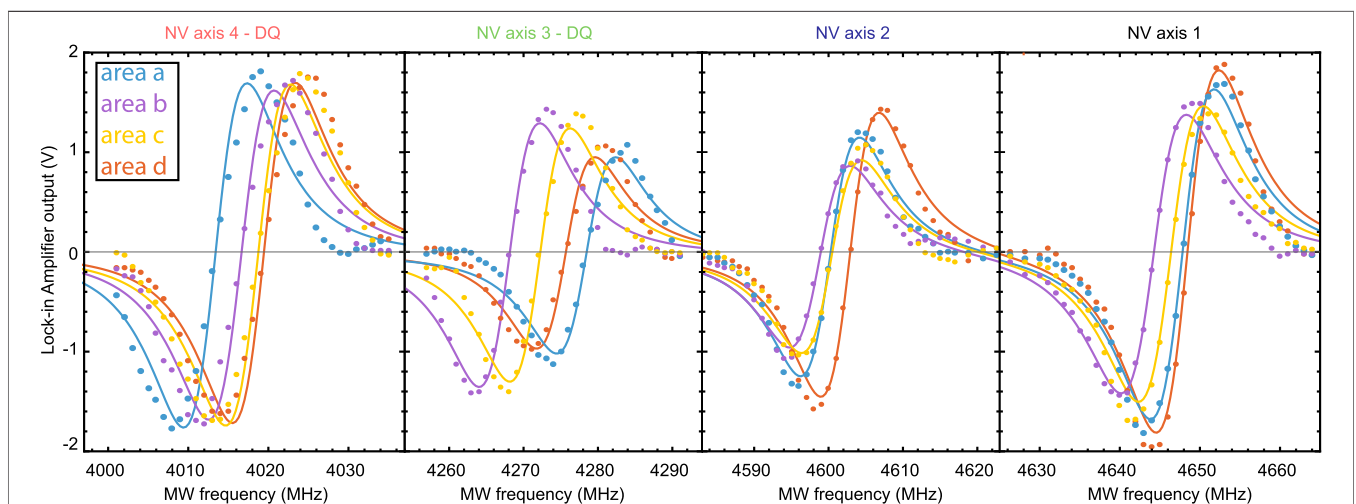
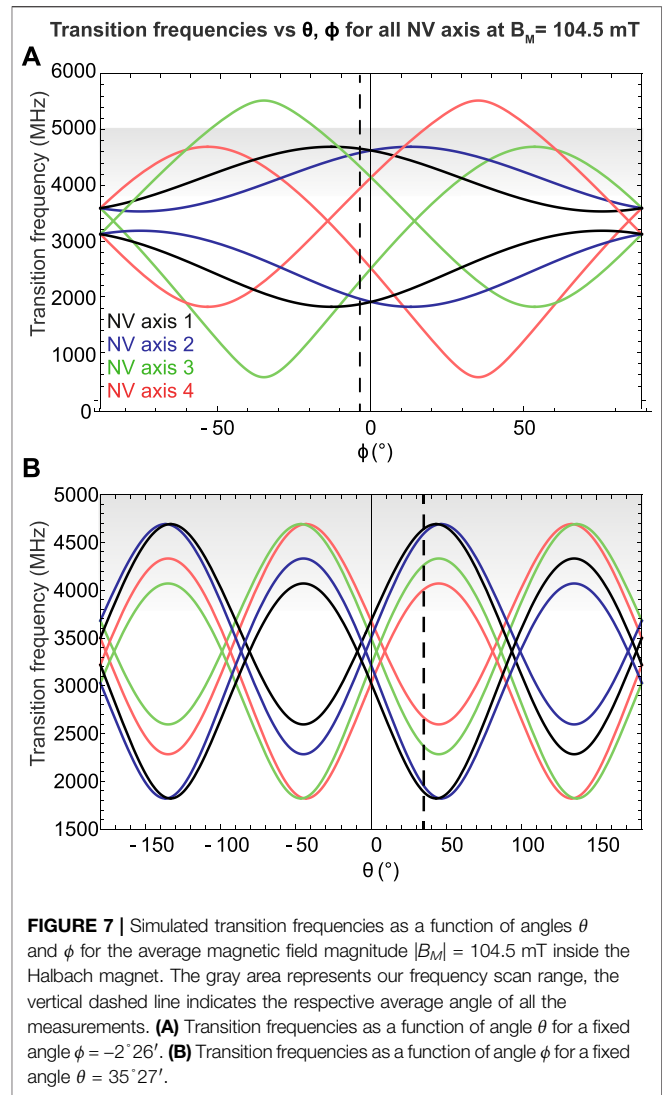
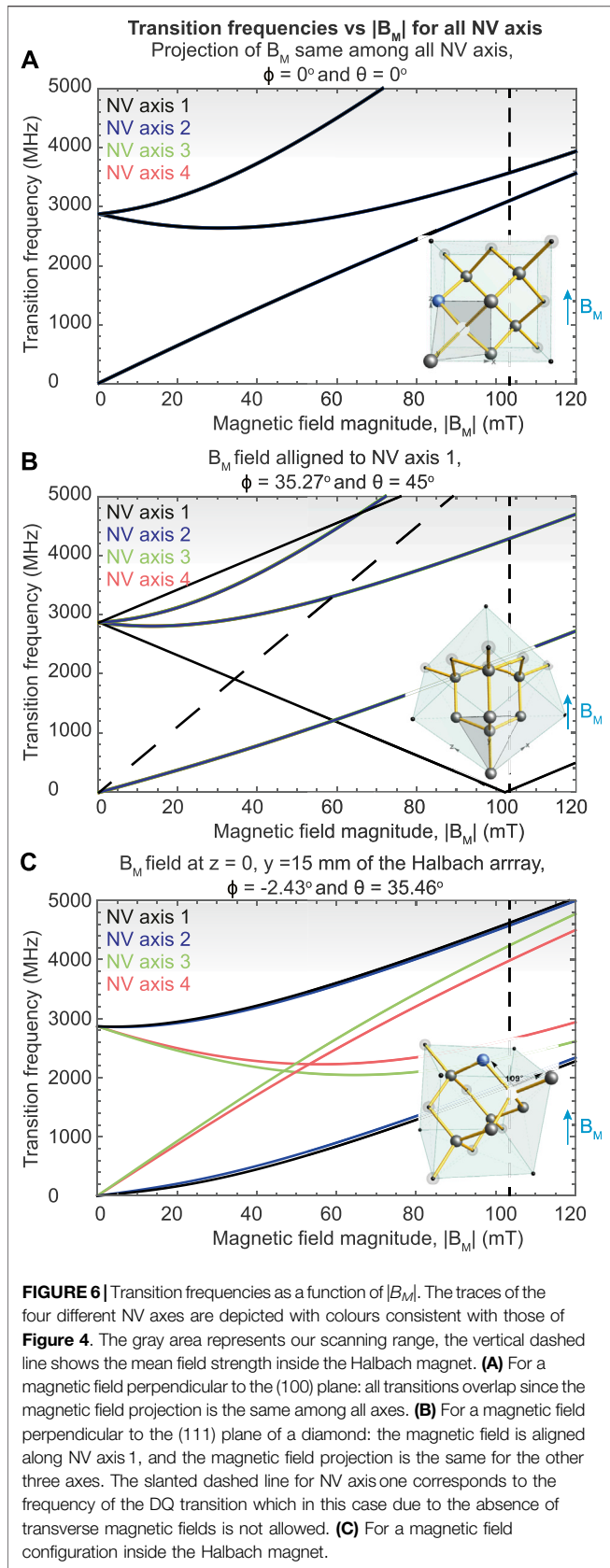
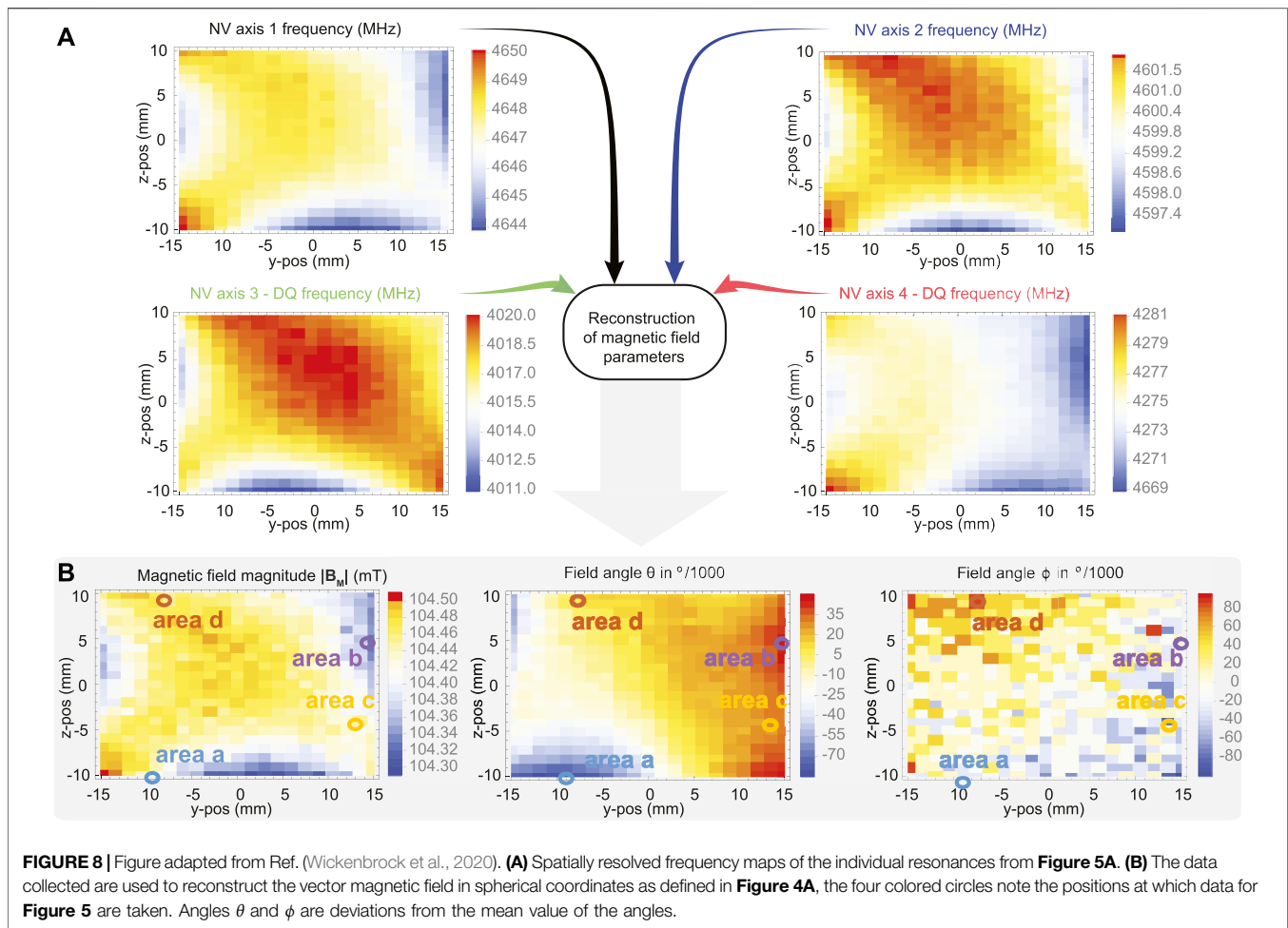


FIGURE 5 | Example data traces of four optically detected resonances at different position near the center of the Halbach magnet. The resonances appear dispersive due to the use of a modulation technique. The resonances are fitted and their center frequencies are extracted. The four different plots correspond to different transitions indicated above the respective plot. The color of the traces indicate the positions at which the data was taken, as seen in Figure 8.



linewidth were fit parameters, an example of the data and fits can be seen in Figure 5. By matching these frequencies to the positions of the 3D translation stages we can make frequency maps as shown in Figure 8A.

To proceed with the analysis and construction of the magnetic field maps we note that the four different features presented in Figure 5 originate from the different NV orientations in the diamond crystal. The positions of these features are related to the alignment of the magnetic field to the NV axis, as well as its amplitude. If the magnetic field is along the NV axis (longitudinal) we observe the $m_s = 0 \rightarrow m_s = \pm 1$ transitions; if there is an additional magnetic field component orthogonal to the NV axis (transverse), transitions between the $m_s = -1$ and $m_s = +1$ are allowed. We call these double quantum (DQ) transitions. For a given magnetic field direction at the position of the sensor, both, the longitudinal and transverse components of the magnetic field are present. Due to mixing caused by the transverse magnetic field component, the NV gyromagnetic ratio depends on the background field strength.



As a result, to match the above frequencies to magnetic fields we create four vectors describing the NV axes. We use parameters β to describe the angle between NV axis and magnetic field and Ω for the field strength. With these parameters we derive a formula which describes the transition frequencies of the spin states, from $m_s = 0$ to $m_s = -1$, as well as $m_s = -1$ to $m_s = +1$ (Rochester & Budker, 2013). Here, we neglect strain and electric field effects.

The frequency of the resonances depends on the magnitude of the magnetic field B_M , as well as the angles θ and ϕ of the diamond orientation with respect to the magnetic field. **Figure 6** shows the resonance frequency dependence as a function of magnetic field magnitude for different fixed angles θ and ϕ . **Figures 6A,B** represent a magnetic field perpendicular to common diamond surface cuts (100) plane for (a) and (111) plane for (b), (c) depicts a configuration inside our Halbach magnet. **Figure 7** shows the dependence of the transition frequencies on the angles θ and ϕ for a magnetic field matching the mean magnitude inside the Halbach magnet. In **Figure 7A** $\phi = -2^\circ 26'$ and θ is varied. In **Figure 7B** $\theta = 35^\circ 27'$ and ϕ is varied.

In both **Figure 6** and **Figure 7** the four different NV axes are depicted with colours matching those in **Figure 4**. We observe that in **Figure 6A** all the transitions overlap, as the projection of the magnetic field is the same among all axes. In **Figure 6B** the

magnetic field is aligned along the NV axis 1, and its projection is the same for the other three axes, which appear overlapped in the figure. The dashed line for NV axis one corresponds to the frequency of the DQ transition which in this case is not allowed, as there is no transverse field on NV axis 1. **Figure 6C** represents a case we encounter while measuring the field inside our Halbach magnet. In **Figure 7**, we note the symmetry between NV axes 1,2 and 3,4 which arises because of the crystallographic structure of the diamond. We can use the information of the above plots to translate the frequency into magnetic field.

After identifying the possible transition frequencies, we use a numerical method to translate the frequencies into magnetic field direction and strength. For this method we restrict the magnetic field strength values to within 10% of what the estimated magnetic field produced by our Halbach array is. Once the magnetic field is calculated for all the different frequencies we express it in polar coordinates. When the initial values for direction and magnitude of the field are approximately known, we find that the reconstruction is unique. We choose B_M to describe the strength of the field, angle θ the latitude angle with respect to the x -axis and ϕ the longitude angle as shown in **Figure 4A**. Finally, we make a list of these parameters and plot

them as shown in **Figure 8B**. In **Figure 8B** we included four different coloured circles to represent the positions at which data for **Figure 5** are taken. The measured averages of angles θ and ϕ in the central $10 \times 5 \text{ mm}^2$ (y-x) of the Halbach magnet are $-2^\circ 26 \pm 1'$ and $35^\circ 2 \pm 1'$, respectively, which is consistent with the orientation of the diamond lattice (cf. **Figure 4**) relative to the coordinate system of the magnet.

5 CONCLUSION AND OUTLOOK

We constructed two fiberized NV based magnetic field sensors. The sensors feature sub-nT/ $\sqrt{\text{Hz}}$ magnetic field sensitivity with high PL-to-pump-light ratio. The components used to make the sensors are commercially available which makes their construction easy and reproducible. The design for the Mainz sensor was made in such a way as to allow free access to the front side of the diamond as well as for robustness, portability, and small size.

With one of the main challenges for NV magnetometry, especially fiberized, being the low photon-collection efficiency, which leads to poor photon-shot-noise limited sensitivity, the 0.5% PL-to-pump-light ratio collection efficiency, demonstrated in the Mainz sensor, can be used to achieve even higher sensitivity, if the effect of other noise sources, e.g. laser-intensity, thermal and magnetic noise, is minimized. This ratio could also be further optimized by implementing side collection on the diamond (Sage et al., 2012; Barry et al., 2020), as well as highly reflective coatings on the opposite (front) side of the diamond. These features were not implemented in this sensor in order to keep all of its components commercial and easily accessible.

The access to the front side of the diamond allows for close proximity to magnetic field sources, which in turn leads to high spatial resolution. The proximity is currently limited to about $300 \mu\text{m}$ by MW wire on top of the diamond. It could be optimized further by using a thinner diamond sample, a sample with shallow implanted NV centers or a thinner MW wire such as, for example, a capton-tape printed circuit board, all depending on the intended application, as these changes influence the sensitivity of the sensor. Such optimization would be especially beneficial for measurements of dipole fields or measurements that require high spatial resolution.

The robustness and portability of the sensors also make them attractive for mapping larger areas, or on-the-move measurements of

magnetic fields. These features combined with the small size of the sensors suggest a use for measuring in hard-to-access places or small areas where maneuverability of the sensor would be required, e.g. endoscopic measurements inside the human body.

As a demonstration of the Mainz sensor we measured the magnetic field of a custom-designed Halbach array. For these measurements, the small fiberized diamond sensor showed a mm-scale spatial resolution, angular resolution of the magnetic field vector extracted in the measurements were $\times 9 \cdot 10^{-3}$ degrees and 18×10^{-3} degrees for angles θ and ϕ , respectively. We note here, that the corresponding displacement due to such a rotation of the diamond sensor (considering a $(0.5 \times 0.5) \text{ mm}^2$ square cross section) could optically not be resolved.

DATA AVAILABILITY STATEMENT

The original contributions presented in the study are included in the article/supplementary material, further inquiries can be directed to the corresponding author/s.

AUTHOR CONTRIBUTIONS

All authors listed have made a substantial, direct, and intellectual contribution to the work and approved it for publication.

FUNDING

This work is supported by the EU FET-OPEN Flagship Project ASTERIQS (action 820394), the German Federal Ministry of Education and Research (BMBF) within the Quantumtechnologien program (grants FKZ 13N14439 and FKZ 13N15064), the Cluster of Excellence “Precision Physics, Fundamental Interactions, and Structure of Matter” (PRISMA + EXC 2118/1) funded by the German Research Foundation (DFG) within the German Excellence Strategy (Project ID 39083149).

ACKNOWLEDGMENTS

We acknowledge Fedor Jelezko for fruitful discussions.

REFERENCES

- Acosta, V. M., Bauch, E., Jarmola, A., Zipp, L. J., Ledbetter, M. P., and Budker, D. (2010). Broadband Magnetometry by Infrared-Absorption Detection of Nitrogen-Vacancy Ensembles in diamond. *APL* 97, 17. doi:10.1063/1.3507884
- Balasubramanian, G., Chan, I. Y., Kolesov, R., Al-Hmoud, M., Tisler, J., Shin, C., et al. (2008). Nanoscale Imaging Magnetometry with diamond Spins under Ambient Conditions. *Nature* 455 (7213), 648–651. doi:10.1038/nature07278
- Barry, J. F., Schloss, J. M., Bauch, E., Turner, M. J., Hart, C. A., Pham, L. M., et al. (2020). Sensitivity Optimization for Nv-diamond Magnetometry. *Rev. Mod. Phys.* 92, 015004. doi:10.1103/revmodphys.92.015004
- Barry, J. F., Turner, M. J., Schloss, J. M., Glenn, D. R., Song, Y., Lukin, M. D., et al. (2016). Optical Magnetic Detection of Single-Neuron Action Potentials

- Using Quantum Defects in diamond. *PNAS* 113, 14133. doi:10.1073/pnas.1601513113
- Chatzidrosos, G., Wickenbrock, A., Bougas, L., Leefer, N., Wu, T., Jensen, K., et al. (2017). Miniature Cavity-Enhanced diamond Magnetometer. *Phys. Rev. Appl.* 8, 044019. doi:10.1103/physrevapplied.8.044019
- Chatzidrosos, G., Wickenbrock, A., Bougas, L., Zheng, H., Tretiak, O., Yang, Y., et al. (2019). Eddy-current Imaging with Nitrogen-Vacancy Centers in diamond. *Phys. Rev. Appl.* 11, 014060. doi:10.1103/physrevapplied.11.014060
- Clevenson, H., Pham, L. M., Teale, C., Johnson, K., Englund, D., and Braje, D. (2018). Robust High-Dynamic-Range Vector Magnetometry with Nitrogen-Vacancy Centers in diamond. *Appl. Phys. Lett.* 112, 252406. doi:10.1063/1.5034216
- Cochrane, C. J., Blacksberg, J., Anders, M. A., and Lenahan, P. M. (2016). Vectorized Magnetometer for Space Applications Using Electrical Readout of Atomic Scale Defects in Silicon Carbide. *Scientific Rep.* 6. doi:10.1038/srep37077

- Dumeige, Y., Chipaux, M., Jacques, V., Treussart, F., Roch, J.-F., Debuisschert, T., et al. (2013). Magnetometry with Nitrogen-Vacancy Ensembles in diamond Based on Infrared Absorption in a Doubly Resonant Optical Cavity. *Phys. Rev. B* 87, 155202. doi:10.1103/physrevb.87.155202
- Dumeige, Y., Roch, J.-F., Bretenaker, F., Debuisschert, T., Acosta, V., Becher, C., et al. (2019). Infrared Laser Threshold Magnetometry with a Nv Doped diamond Intracavity Etalon. *arXiv:2008.07339* 27, 1706–1717. doi:10.1364/oe.27.001706
- Hadden, J. P., Harrison, J. P., Stanley-Clarke, A. C., Marseglia, L., Ho, Y.-L. D., Patton, B. R., et al. (2010). Strongly Enhanced Photon Collection from diamond Defect Centers under Microfabricated Integrated Solid Immersion Lenses. *APL* 97, 241901. doi:10.1063/1.3519847
- Jensen, K., Leefer, N., Jarmola, A., Dumeige, Y., Acosta, V. M., Kehayias, P., et al. (2014). Cavity-enhanced Room-Temperature Magnetometry Using Absorption by Nitrogen-Vacancy Centers in diamond. *Phys. Rev. Lett.* 112, 160802. doi:10.1103/physrevlett.112.160802
- Kucsko, G., Maurer, P. C., Yao, N. Y., Kubo, M., Noh, H. J., Lo, P. K., et al. (2013). Nanometre-scale Thermometry in a Living Cell. *Nature* 500, 54–58. doi:10.1038/nature12373
- Lovchinsky, I., Sushkov, A. O., Urbach, E., Leon, N. P. d., Choi, S., Greve, K. D., et al. (2016). Nuclear Magnetic Resonance Detection and Spectroscopy of Single Proteins Using Quantum Logic. *Science* 351, 836. doi:10.1126/science.aad8022
- Maze, J. R., Stanwix, P. L., Hodges, J. S., Hong, S., Taylor, J. M., Cappellaro, P., et al. (2008). Nanoscale Magnetic Sensing with an Individual Electronic Spin in diamond. *Nature* 455 (7213), 644–647. doi:10.1038/nature07279
- Patel, R. L., Zhou, L. Q., Frangeskou, A. C., Stimpson, G. A., Breeze, B. G., Nikitin, A., et al. (2020). Sub-nanotesla Magnetometry with a Fibre-Coupled diamond Sensor. *Phys. Rev. Appl.* 14, 044058. doi:10.1103/PhysRevApplied.14.044058
- Rittweger, E., Han, K. Y., Irvine, S. E., Eggeling, C., and Hell, S. W. (2009). Sted Microscopy Reveals crystal Colour Centres with Nanometric Resolution. *Nat. Photon.* 3 (3), 144–147. doi:10.1038/nphoton.2009.2
- Rochester, S., and Budker, D. (2013). NV Centers in diamond. *online tutorial*. Available at: <http://budker.berkeley.edu/Tutorials/index.html>.
- Sage, D. L., Pham, L. M., Bar-Gill, N., Belthangady, C., Lukin, M. D., Yacoby, A., et al. (2012). Efficient Photon Detection from Color Centers in a diamond Optical Waveguide. *Phys. Rev. B* 85, 121202. doi:10.1103/physrevb.85.121202
- Siyushev, P., Kaiser, F., Jacques, V., Gerhardt, I., Bischof, S., Fedder, H., et al. (2010). Monolithic diamond Optics for Single Photon Detection. *APL* 97, 241902. doi:10.1063/1.3519849
- Stürner, F. M., Brenneis, A., Buck, T., Kassel, J., Rölver, R., Fuchs, T., et al. (2021). Integrated and Portable Magnetometer Based on Nitrogen-Vacancy Ensembles in diamond. *Adv. Quantum Technol.* 4 (4), 2000111. doi:10.1002/qute.202000111
- Wickenbrock, A., Zheng, H., Bougas, L., Leefer, N., Afach, S., Jarmola, A., et al. (2016). Microwave-free Magnetometry with Nitrogen-Vacancy Centers in diamond. *Appl. Phys. Lett.* 109, 053505. doi:10.1063/1.4960171
- Wickenbrock, A., Zheng, H., Chatzidrosos, G., Rebeiro, J. S., Schneemann, T., and Bluemler, P. (2021). High Homogeneity Permanent Magnet for diamond Magnetometry. *arXiv:2008.07339* 322, 106867. doi:10.1016/j.jmr.2020.106867
- Wolf, T., Neumann, P., Nakamura, K., Sumiya, H., Ohshima, J., and Isoya, T., et al. (2015). Subpicotesla diamond Magnetometry. *Phys. Rev. X* 5, 041001. doi:10.1103/physrevx.5.041001
- Xie, Y., Yu, H., Zhu, Y., Qin, X., Rong, X., Duan, C.-K., et al. (2021). A Hybrid Magnetometer towards Femtotesla Sensitivity under Ambient Conditions. *Sci. Bull.* 66, 127. doi:10.1016/j.scib.2020.08.001
- Zhang, C., Shagieva, F., Widmann, M., Kübler, F., Vorobyov, V., Kapitanova, P., et al. (2021). Diamond Magnetometry and Gradiometry towards Subpicotesla Dc Field Measurement. *Phys. Rev. Appl.* 15, 064075. doi:10.1103/physrevapplied.15.064075
- Zheng, H., Chatzidrosos, G., Wickenbrock, A., Bougas, L., Lazda, R., Berzins, A., et al. (2017). Level Anti-crossing Magnetometry with Color Centers in diamond. *Proc. SPIE*, 10119, 101190X. doi:10.1117/12.2261160
- Zheng, H., Sun, Z., Chatzidrosos, G., Zhang, C., Nakamura, K., Sumiya, H., et al. (2020). Microwave-free Vector Magnetometry with Nitrogen-Vacancy Centers along a Single axis in diamond. *Phys. Rev. Appl.* 13, 044023. doi:10.1103/physrevapplied.13.044023

Conflict of Interest: Authors AB, FS, TF, TB, and RR were employed by the company Robert Bosch GmbH.

The remaining authors declare that the research was conducted in the absence of any commercial or financial relationships that could be construed as a potential conflict of interest.

Publisher's Note: All claims expressed in this article are solely those of the authors and do not necessarily represent those of their affiliated organizations, or those of the publisher, the editors and the reviewers. Any product that may be evaluated in this article, or claim that may be made by its manufacturer, is not guaranteed or endorsed by the publisher

Copyright © 2021 Chatzidrosos, Rebeiro, Zheng, Omar, Brenneis, Stürner, Fuchs, Buck, Rölver, Schneemann, Blümmler, Budker and Wickenbrock. This is an open-access article distributed under the terms of the Creative Commons Attribution License (CC BY). The use, distribution or reproduction in other forums is permitted, provided the original author(s) and the copyright owner(s) are credited and that the original publication in this journal is cited, in accordance with accepted academic practice. No use, distribution or reproduction is permitted which does not comply with these terms.